

**COVER SHEET**

Paper Number: **28854**

Title: **Damage Mechanisms in Tapered Composite Structures under Static and Fatigue Loading**

Authors: Prabhakar M. Rao<sup>1</sup>  
Mark R. Gurvich<sup>1</sup>  
Upul R. Palliyaguru<sup>2</sup>  
Waruna Seneviratne<sup>2</sup>

## **ABSTRACT**

In this work an integrated computational/experimental approach was developed to validate the predictive capabilities of State-of-the-Art (SoA) Progressive Damage Analysis (PDA) methods and tools. Specifically, a tapered composite structure incorporating ply-drops typical in the aerospace industry to spatially vary structural thickness was tested under static tension and cyclic tension fatigue loads. The data acquired from these tests included quantitative metrics such as pre-peak stiffness, peak load, location of delamination damage onset, and growth of delaminations as functions of applied static and fatigue loads. It was shown that the PDA tools were able to predict the pre-peak stiffness and peak load within  $\pm 10\%$  of experimental average, thereby meeting and exceeding the pre-defined success criteria. Additionally, it was shown that the PDA tools were able to accurately predict the location of delamination onset and satisfactorily predict delamination growth under static tension loading. Overall, good correlations were achieved between modeling and experiments.

## **INTRODUCTION**

In composite aerospace structures, manufacturing artifacts such as ply-drops are often used to spatially vary thickness in lieu of machining. However, such artifacts represent large-scale discontinuities which lead to sharp gradients in the stress fields and corresponding stress concentrations. Therefore, damage is typically found to onset in the vicinity of ply-drops and is often characterized by matrix cracking in off-axis plies resulting in inter-laminar delaminations. As a result, the capability to computationally predict damage onset at manufacturing discontinuities and thereby enable structurally durable and geometrically complex composite parts becomes critically important. This effort, therefore, is focused on the development, and verification and validation (V&V) of Progressive Damage Analysis (PDA) methods and tools, developed within NASA Advanced Composites Project (ACP), to enable the design and reduce the certification timeline of composite aerospace structures.

- 
- 1. United Technologies Research Center, 411 Silver Lane, East Hartford, CT 06108.**
  - 2. National Institute for Aviation Research, Wichita State University, 1845 Fairmount St., Wichita, KS 67260.**

The classic building block V&V approach adopted herein is illustrated in Figure 1. Essentially, the idea is to verify and validate the PDA tools at lower length scales while moving up the building block. Several studies [1–5] have been reported in the literature that provide detailed discussions on the V&V of PDA techniques at the ‘Coupon’ level of the building approach, Figure 1. Also, as part of the ACP, validation of PDA codes at the ‘Sub-elements’ level, Figure 1, based on Continuum Damage Mechanics (CDM) [6] and Discrete Damage Mechanics (DDM) [7, 8] techniques have been reported.

The broader goal of the ACP program is to achieve independent V&V of PDA codes at the ‘Elements’ level, Figure 1. For this purpose, a three-dimensional (3D) tapered laminated composite structure incorporating a racetrack cross-section, Figure 1, has been designed, analyzed, and fabricated. The chosen structural geometry, Figure 1, is representative of rotor blade composite spars which experience tensile, cyclic bending and torsional loads in service. As a result, the blade spar element, Figure 1, may exhibit potentially interacting damage modes, thereby, making it difficult to isolate delamination onset and growth.

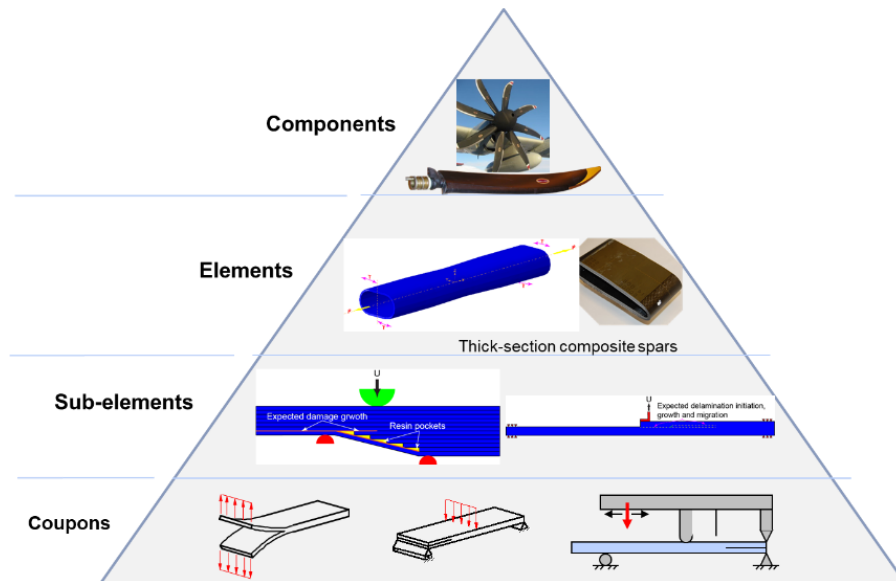


Figure 1. The building block approach for validating Progressive Damage Analysis (PDA) codes.

In a previous study conducted by the authors [9], a quasi-2D control specimen, namely, the blade spar pathfinder test article was designed, analyzed, fabricated and initially tested under displacement-controlled axial static tension loads. The pathfinder test article [9], Figure 2, incorporates a tapered cross-section geometry and is fabricated with IM7/8552 unidirectional tape material using an autoclave process. The objective of the present work therefore, is to demonstrate the ability to experimentally capture delamination onset and growth from the vicinities of the ply-drops in the pathfinder test article, Figure 2. Based on the previous work of the authors [9], it is expected that delamination onset and growth in the pathfinder test article, would occur from the vicinities of the first ply-drop(s) on either side of the central thin region, Figure 2.

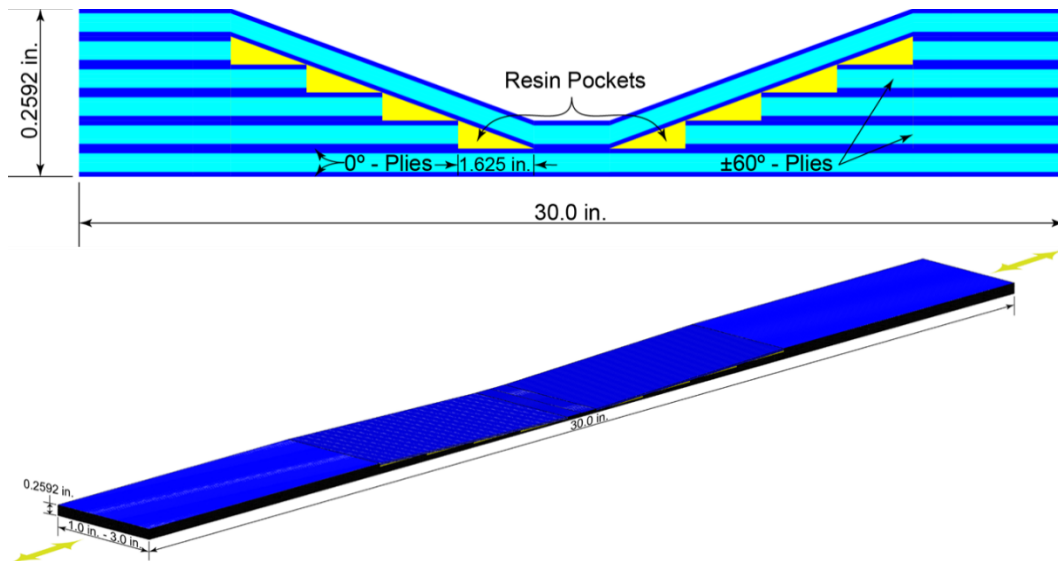


Figure 2. The composite pathfinder element with ply-drops showing resin pockets and continuous plies

Towards achieving the above goals, the pathfinder test article, Figure 2, was tested under displacement-controlled static tension and load-controlled cyclic tension. The static tests yielded load-displacement and load-strain data as well as Ultrasonic (UT) images documenting the onset and growth of delaminations from the expected locations. A more specific objective of the current study is to validate blind predictions of the static response of the pathfinder test article, obtained using two PDA codes, namely, CompDam [10] and the Floating Node Method (FNM) [11]. However, only the validations and correlations based on load-displacement data and UT images are reported. Fatigue tests yielded C-Scan images documenting the onset and growth of delaminations from the expected locations and delamination growth as functions of applied loading cycles. Validation of the predicted fatigue response of the pathfinder article is a work-in-progress and is not reported herein.

## PATHFINDER TESTING

### Test Setup



Figure 3. Pathfinder test setup.

The pathfinder article was tested at the National Institute for Aviation Research (NIAR), Wichita State University (WSU), Figure 3. The pathfinder article was instrumented with strain gages and Acoustic Emission (AE) sensors. The AE data was used as a reference to intermittently stop the test and acquire through-thickness UT images to characterize delamination growth.

### Outcomes of Static Testing

A total of three static tests were performed under displacement control. Two (2) repeats were performed on specimens measuring 3.0 in. wide, while one (1) repeat was performed on a specimen measuring 1.0 in. wide. The total load normalized by the specimen width,  $w$ , is presented as a function of the applied displacement in Figure 4.

Until the attainment of peak load, Figure 4, the response of the pathfinder is linear. The post-peak response is characterized by a sudden load drop, Figure 4, indicative of unstable fracture resulting from extensive matrix cracking and fiber failure. Through-thickness UT images obtained at progressively increasing load levels, Figure 5, show that delamination onset is observed at  $P_{Total}^{Max} = 22489 \text{ lbf}$  or  $p = P_{Total}^{Max}/3.0 = 7496 \text{ lbf/in.}$  which is very close to the recorded peak load,  $P_{Total}^{Max} = 22752 \text{ lbf}$  or  $p = P_{Total}^{Max}/3.0 = 7584 \text{ lbf/in.}$  However, as seen in Figure 5, the delamination onset is more pronounced on one side, alluding to the non-symmetric response of the pathfinder article.

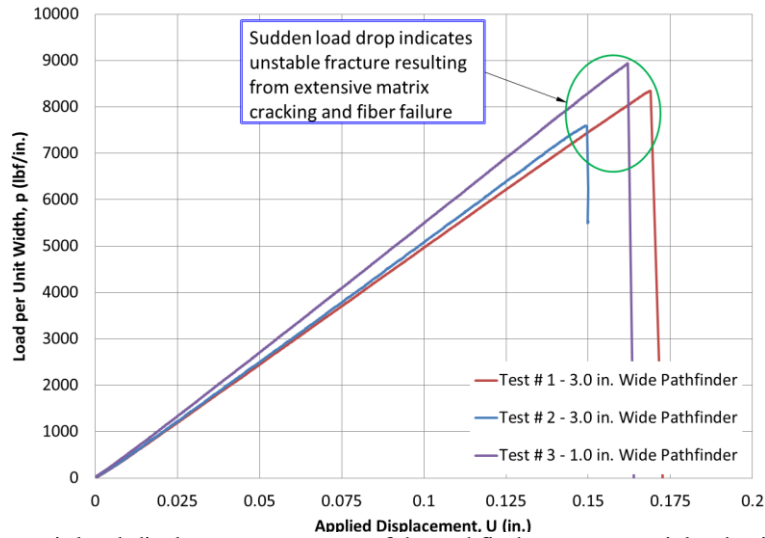


Figure 4. The static load-displacement response of the pathfinder spar test article obtained at NIAR.

Additionally, post-test photographs obtained upon the completion of Test # 1 and Test # 2, exhibit delamination, matrix cracking and fiber breakage damage modes, as shown in Figure 6. The side views of the pathfinder test article, Figure 6 (a), imply that cracks at the tips of dropped plies migrated to the immediate top and bottom interfaces resulting in the large-scale delaminations documented therein. The damage patterns documented in Figure 6 (b) indicate that belt and core plies only delaminate and detach from the dropped ply blocks. Furthermore, matrix cracking and fiber breakage is confined to the thin central region (see Figure 2) of the pathfinder article. It is well-known that delamination onset and growth are not generally associated with any significant load-drop, as discussed elsewhere [12]. Therefore, the recorded sudden load drops indicative of unstable fracture, result from the damage characterized by extensive matrix cracking and subsequent fiber breakage, Figure 6.

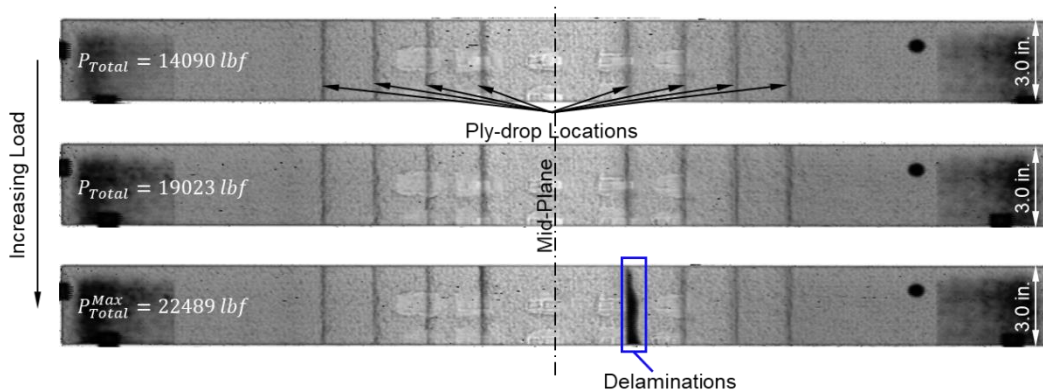


Figure 5. Through-thickness interval UT images obtained during Test # 2 exhibiting the location and subsequent growth of delaminations.

Overall, the above discussions indicate that the expected damage modes were successfully captured in the pathfinder test article. Specifically, matrix cracking in the vicinity of the ply-drop regions leads to delamination initiation, onset and growth, while the ultimate failure of the pathfinder article is characterized by extensive intra-ply

matrix cracking and subsequent fiber breakage. The data in Figure 4 were used for quantitative validation of the predictions obtained with PDA codes. On the other hand, UT images in Figure 5, and post-test photographs in Figure 6 were used for qualitative validation of the predictions obtained with PDA codes.

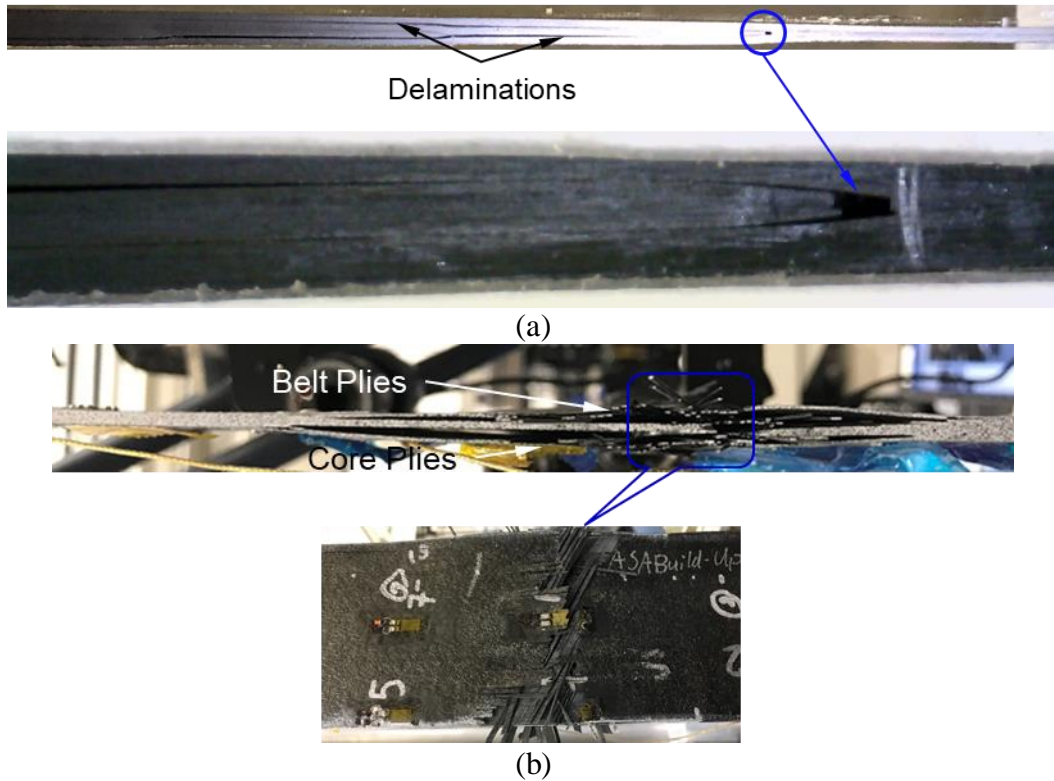


Figure 6. Post-test photographs. (a) Evidence of large scale delaminations obtained upon completion. (b) Evidence of delaminations, matrix cracking and fiber.

### Outcomes of Fatigue Testing

The pathfinder test article, characterized by width,  $w = 1.0 \text{ in.}$ , was tested under tension-tension fatigue loading at R-ratio defined as:  $R = P_{Min}/P_{Max} = 0.10$  and a loading frequency:  $f = 2 \text{ Hz}$ . A total of five (5) repeats were performed. Three repeats were performed with  $P_{Max} = 5000 \text{ lbf}$  which is  $\sim 60\%$  of the average static peak load,  $P_{Exp}^{Avg} = 8263 \text{ lbf}$ . Additionally, two (2) repeats were performed with  $P_{Max} \approx 0.55 P_{Exp}^{Avg} = 4500 \text{ lbf}$ . The fatigue tested pathfinder specimens were not instrumented with strain gages, but interval through-thickness C-Scan images were obtained to monitor the location and mode of damage onset and subsequent growth.

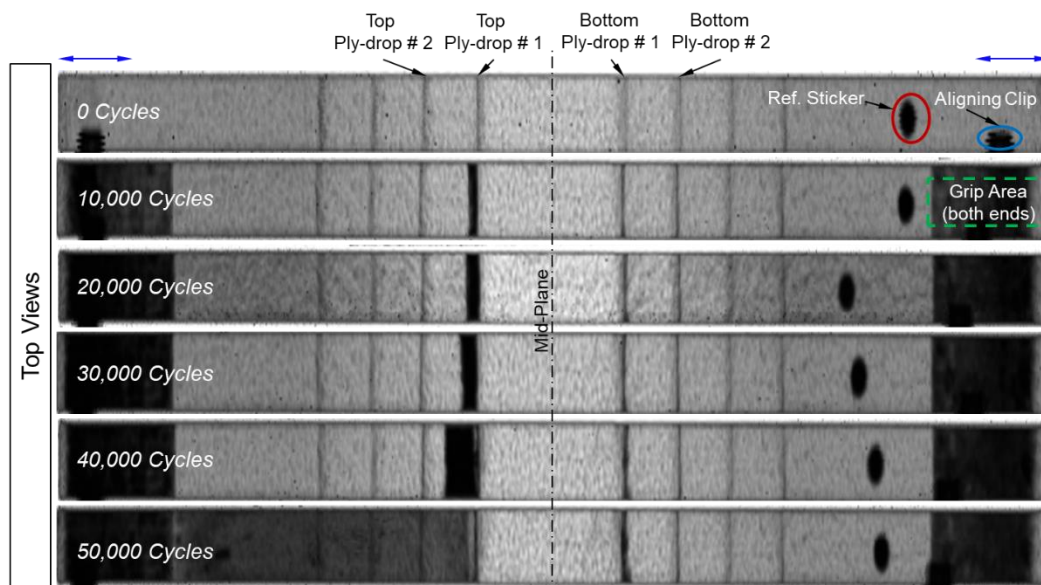


Figure 7. UT images obtained at NIAR showing the location of delamination onset and direction growth as a function of loading cycles.

The outcomes of the first pathfinder fatigue test are shown in Figure 7. It is evident that the first delamination onset is recorded at the first ply-drop on one side of the mid-plane, consistent with the observations based on static testing, Figure 5. The first delamination onset is observed at 10,000 cycles, albeit on the opposite of the mid-plane relative to the static test outcome, Figure 5. While this result contradicts static test outcomes, it is important to note that, the first delamination onset is recorded at the first ply-drop off the mid-plane – consistent with the design intent of the pathfinder [9]. Randomness in the location of delamination onset could be attributed to local variations in the geometry and potentially microstructure, imparted by the manufacturing process. With continued load cycling, this initial delamination grows further to the left, Figure 7, and by 50,000 cycles, it has grown to the end of specimen. In parallel, delamination onset is also recorded to the right side of the mid-plane at 20,000 cycles, Figure 7. However, this delamination does not grow as extensively as the one on the left side of the mid-plane, perhaps as a result of the above stated local variations.



Figure 8. Post-test photographs of the fatigue tested specimen at NIAR showing the location and extent of delamination growth.

The C-Scan images in Figure 7 do not lend themselves to deciphering at which interface in the through-thickness direction, the delaminations are growing. Post-test photographs showing the side views of the specimen in Figure 7 are presented in Figure 8. These pictures present clear evidence of the location and extent of delamination growth, consistent with the design intent of the pathfinder [9]. The remainder of the fatigue tests resulted in similar damage modes and growth characteristics. However, for the sake of brevity only select outcomes are reported herein.

In addition to documenting damage modes, the data obtained via C-Scan images was post-processed to obtain delamination growth as a function of applied cyclic loading. The procedure involved measuring the area of the delamination using the C-Scan image data (see Figure 7) and dividing it by the width of the specimen,  $w = 1.0 \text{ in}$ . For example, consider the C-Scan image of the specimen in Figure 7 at 40,000 cycles wherein the individual delamination extents can be represented as three unique areas,  $A_1^L$ ,  $A_1^R$  and  $A_2^R$ , Figure 9 – the superscripts  $L$  and  $R$  are used to locate delamination extents to the left and right of the mid-plane.

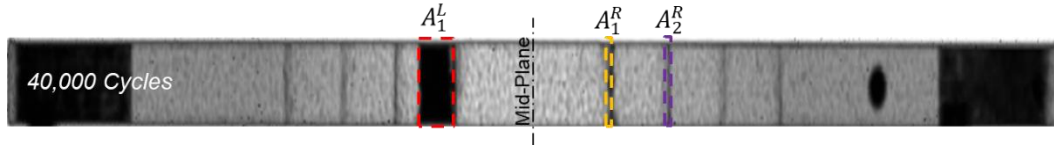


Figure 9. Delamination extents at 40,000 cycles.

The subscripts in the above nomenclature also indicate the number of unique delaminations that are onset and grow on either side of the mid-plane. For the specimen in Figure 7, the output of the above post-processing procedure is presented in Table I.

TABLE I. DELAMINATION EXTENTS AS FUNCTIONS OF LOADING CYCLES

Cycle Count (N)	$A_1^L$ (in <sup>2</sup> )	$A_1^R$ (in <sup>2</sup> )	$A_2^R$ (in <sup>2</sup> )
0	0.00	0.00	0.00
10000	0.23	0.00	0.00
20000	0.34	0.01	0.00
30000	0.44	0.02	0.00
40000	0.90	0.07	0.00
50000	8.22	0.20	0.01

The data in Table I indicates that the length of the major delamination on the left side of the mid-plane (see Figure 7) grows gradually up to 40000 loading cycles and then its growth rate increases suddenly. At 50000 cycles or end-of-life, the major delamination measures  $\ell_1^L = A_1^L/w = 8.22 \text{ in}$ .

Following the above procedure, delamination growth was measured as a function of applied loading cycles in all the five (5) specimens tested as part of this study. This cumulative dataset is shown in Figure 10. Regardless of  $P_{Max}$ , the data in Figure 10 indicate initial progressive growth of the delaminations at a gradual rate, followed by very fast growth rate, which is reminiscent of static growth. The recorded scatter in the data in Figure 10 is typical of fatigue testing.

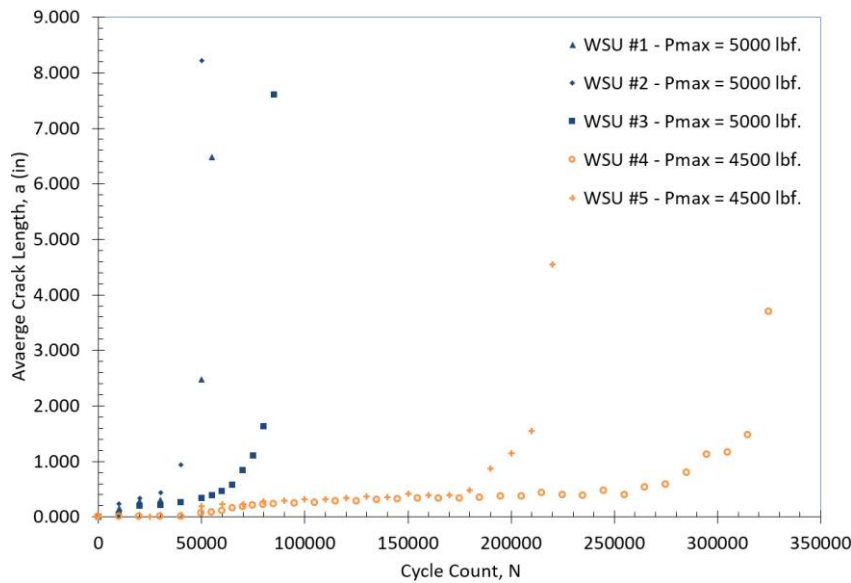


Figure 10. Delamination growth recorded as a function of applied loading cycles.

## FINITE ELEMENT MODELING OF THE PATHFINDER TEST ARTICLE

The static and fatigue testing outcomes indicate that the damage response of the pathfinder test article is not symmetric. However, delamination onset begins from the first ply-drop off the mid-plane, consistent with the design intent [9]. Therefore, for maintaining tractability of the solutions, only one-half of the pathfinder test article was modeled, without including any manufacturing-induced local inconsistencies. Validation of two PDA codes, namely, CompDam [10] and the Floating Node Method (FNM) [11] was performed in the current study, using outcomes of the testing effort discussed in the previous sections. The CompDam model of the pathfinder test article was 3.0 in. wide, whereas, the FNM model of the same article was 1.0 in. wide.

### CompDam Model of the Pathfinder

The CompDam code implements a Vectorized User-defined Material model (VUMAT) in ABAQUS/Explicit [13] based on Deformation Gradient Decomposition (DGD) [10]. Matrix crack initiation is predicted using the LaRC04 [14] criteria, while matrix crack kinematics are addressed by treating them as cohesive surfaces embedded in a deformable continuum. In the current validation effort, the composite plies i.e. the deformable continua, and resin pockets in the pathfinder article were discretized with reduced integration continuum elements. Each element was chosen to have in-plane dimensions of 0.0394 in. (1.00 mm) length and 0.0394in. (1.00 mm) width, in order to achieve mostly square elements. The thickness of each element discretizing the composite plies was taken to be equal to the ply thickness i.e. 0.0072 in. (0.183 mm). It is recognized that the in-plane element dimensions are larger than those suggested elsewhere [15], but, it should be noted that very small element sizes may not be practical from the standpoint of inclusion in aerospace structures.

A 2D schematic representation of the meshing strategy is shown in Figure 11. Therein, Figure 11, the dark blue regions indicate on-axis  $0^\circ$  plies, whereas, the light

blue regions exhibit the locations of the off-axis  $\pm 60^\circ$  plies. The on- and off-axis plies are located within individual ply blocks i.e. Block # 1 through Block # 6, Figure 11. Specifically, Block # 1 includes the core plies, while Block # 6 incorporates the belt plies. The resin pockets are shown as yellow regions in Figure 11 and labeled RP # 1 through RP # 4. The interface regions between the resin pockets and the tips of the corresponding dropped ply block are labeled RP1/B2 Interface through RP4/B5 Interface, Figure 11. The inter-laminar region between the tapered portion of Block # 6 and the upper surface of the resin pockets is labeled Tapered Interface, Figure 11.

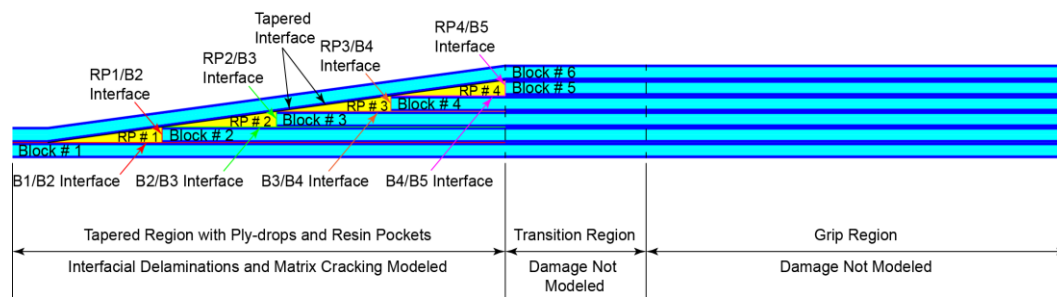


Figure 11. Schematic representation of the meshing strategy adopted for modeling the pathfinder spar test article using the CompDam code.

CompDam requires directionally oriented or fiber-aligned meshes to accurately capture the orientation of matrix cracks. For this purpose, a user-developed Python program was used to model the off-axis plies, include requisite cohesive elements in the interfacial regions and define appropriate tie constraints to connect individual plies to the interface regions within the pathfinder article. The neat resin pockets were modeled using native ABAQUS [13] capabilities and were joined to the fiber-aligned plies and inter-laminar cohesive elements via appropriate tie constraints. Damage is modeled only within the tapered region, as indicated in Figure 11. Specifically, matrix cracking is captured within the on- and off-axis plies in the tapered region, and delaminations are captured at the individual interfaces shown in Figure 11. The 3D Finite Element (FE) mesh of the pathfinder developed using the above techniques is shown in Figure 12. The bottom, vertical and tapered surfaces of the triangular prismatic resin pockets are each connected to respective layers of zero-thickness cohesive elements using surface-based tie constraints. This modeling feature allows capturing delaminations between resin pockets and ply blocks and cracks at the interface between the tips of dropped ply blocks and resin pockets, as shown for instance in Figure 6.

Furthermore, matrix cracking is captured in the on- and off-axis plies with the crack spacing parameter set to 4. The crack spacing parameter is internal to CompDam and allows the user to control the spatial distribution of matrix cracks in the deformable continuum. As a result, matrix cracking is captured in every fourth row of red colored elements in the on- and off-axis plies, Figure 12 – the blue colored elements in Figure 12 are not damaged. Based on experimental evidence, Figure 6, it can be reasoned that the belt plies (i.e. Block # 6, Figure 11) detach or delaminate from the rest of the structure without exhibiting any significant damage in the tapered regions. Therefore, damage in the tapered region of the belt plies is not modeled in the current effort. The 3D FE mesh in Figure 12 is composed of a total of 1,834,602 nodes and 968,044 elements, leading to 5,525,184 degrees of freedom.

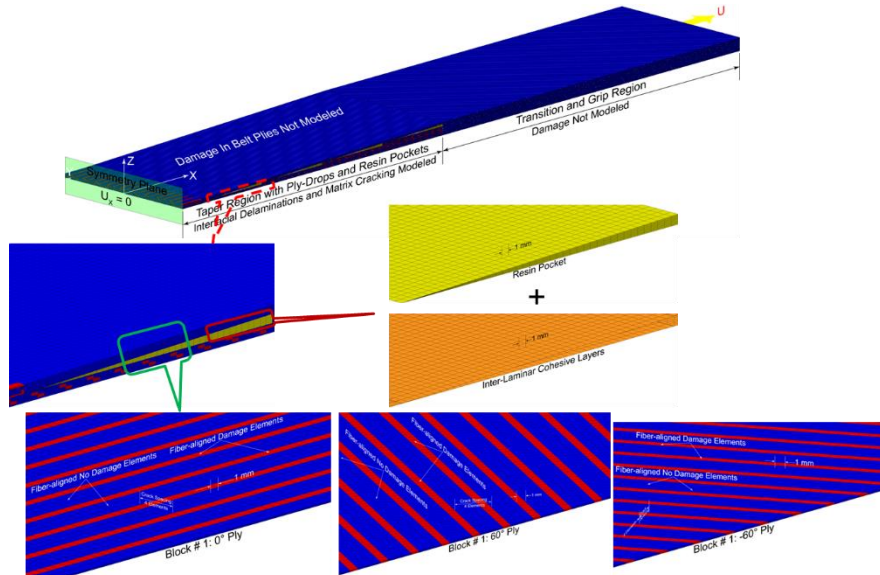


Figure 12. Schematic representation of the meshing strategy adopted for modeling the pathfinder spar test article using the CompDam code.

Since the simulations were executed using an explicit code (CompDam), the total time,  $t = 0.25$  seconds with the objective that the total number of increments,  $N_{INC} \leq 1,500,000$ , leading to,  $dt = t/N_{INC} = 1.67 \times 10^{-07}$  seconds. In order to achieve the above objectives, both Fixed Mass Scaling (FMS) and Variable Mass Scaling (VMS) [13] algorithms were used to speed up the associated quasi-static simulations. ABAQUS/Explicit [13] was instructed to perform FMS at the beginning of the step, whereas VMS was invoked to scale the mass of the entire model at a frequency of 100 increments such that the minimum stable time increment,  $dt_{min}^{stable} \geq 1.5 \times 10^{-07}$  seconds. The mass scaling factors were automatically calculated by ABAQUS/Explicit [13] based on the specifications related to the FMS and VMS algorithms. While ABAQUS/Explicit [13] was able to maintain,  $dt_{min}^{stable} \geq 1.5 \times 10^{-07}$  seconds, the analysis terminated at the simulation time,  $t = 0.1235$  seconds, due to excessive element distortion.

### FNM Model of the Pathfinder

The FNM implements a 48-node 3D User-defined Element (UEL) in ABAQUS/Standard [13]. Fundamental aspects of the FNM can be found for instance, in [11]. More recently [8], the FNM was used to model tapered composite three-point bending specimens under static and fatigue loading conditions. Each FNM UEL is composed of two solid sub-elements and an embedded interface element, as shown on the left in Figure 13. Additional nodes (Floating Nodes) and additional degrees of freedom (Floating Degrees of Freedom (DOFs)) are added to the above regular finite elements. The Floating Nodes and Floating DOFs are linked to the crack path within the element as shown for instance on the right in Figure 13. As a result, the FNM addresses matrix crack kinematics by splitting finite elements used to discretize deformable continua. Crack growth under static loading conditions is modeled via traction-separation cohesive laws, whereas, the same under fatigue loading is modeled using the Paris Law.

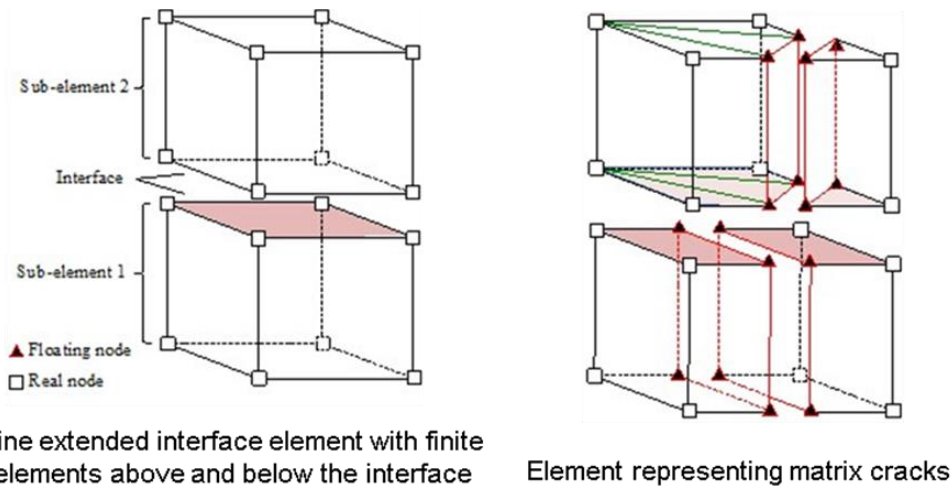


Figure 13. Conceptual schematics illustrating the pristine FNM UEL (left) and the cracked FNM UEL (right).

In the current validation effort, the composite plies and resin pockets in the pathfinder article were discretized with 3D elements 0.0394 in. (1.00 mm) long and 0.0394 in. (1.00 mm) wide, in order to achieve mostly square elements. The thickness of each element discretizing the composite plies was taken to be equal to the ply thickness i.e. 0.0072 in. (0.183 mm). In order to introduce FNM UELs in the 3D FE mesh, the volume of the pathfinder article was divided into a ‘local’ FNM region and a ‘global’ native ABAQUS [13] region. Each of these regions was meshed separately and subsequently connected via tie constraints defined using node-based slave and element-based master surfaces. Schematics illustrating the geometry of the local and global regions are shown in Figure 14.

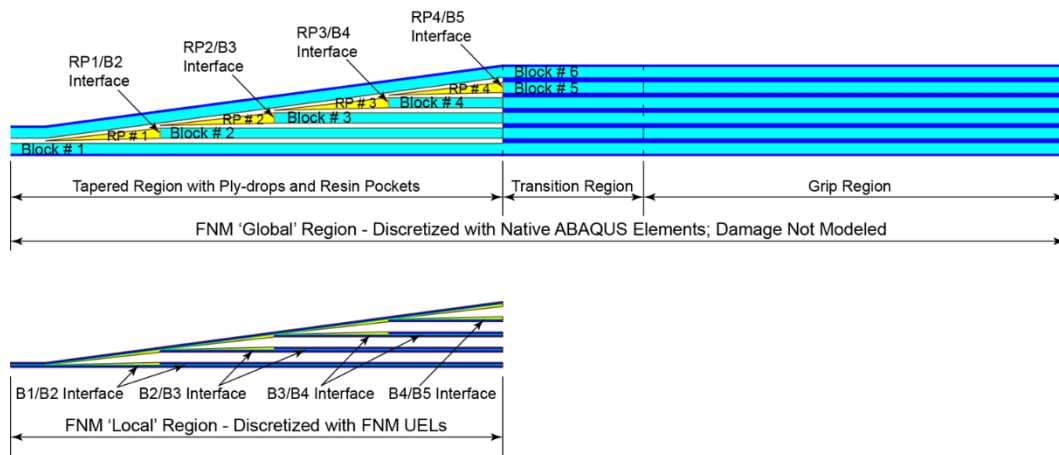


Figure 14. Schematic representation of the meshing strategy adopted for modeling the pathfinder spar test article using the FNM code.

The ‘local’ region in Figure 14 essentially fits into the ‘global’ region. Subsequently, node-based surfaces are defined along the outer peripheries of the ‘local’ and element-based surfaces are defined along the inner peripheries of the ‘global’ region which are connected via tie constraints. Delaminations are captured along the interfaces labeled

B1/B2 Interface through B4/B5 Interface, Figure 14, while matrix cracks are captured in the dark blue regions incorporating  $0^\circ$  plies within the ‘local’ regions. By design, matrix cracks are not captured in the off-axis plies in the FNM model of the pathfinder. It is recognized that this modeling feature is a limitation, but it will be overcome in future efforts.

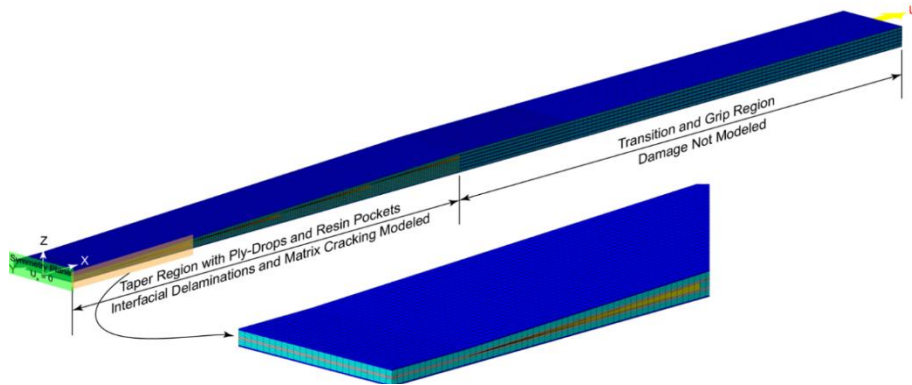


Figure 15. The complete FNM mesh of the pathfinder article. The zoomed-in region shows the ‘local’ region in grey color for clarity.

The complete FNM mesh of the pathfinder article is shown in Figure 15. This mesh is composed of 243,975 elements which includes 14,675 FNM UELs while the remainder 229,300 are native ABAQUS [13] elements. The total number of nodes in the model is 536,096 resulting in 1,611,174 degrees of freedom. The local regions composed of FNM UELs were first meshed with native ABAQUS elements and subsequently, this native ABAQUS mesh was converted to a FNM mesh using a user-developed Python program. In order to capture matrix cracks between the ends of the dropped plies and the resin pockets ahead of the same (see Figure 6), native ABAQUS cohesive elements were introduced into the mesh.

## MODEL-TEST CORRELATIONS

### Comparisons of the Load-Displacement Response

The static load-displacement response computed by CompDam and FNM is correlated with experimental data and presented in Figure 16. Evidently, the pre-peak stiffness within the solution domain  $0.030 \text{ in.} \leq U \leq 0.205 \text{ in.}$ , is predicted well within the pre-established  $\pm 10\%$  bounds. The experimentally determined average peak load normalized by the width of the pathfinder spar article is  $p_{Exp}^{Avg} = 8,263 \text{ lbf/in.}$  The peak load predicted by CompDam is  $p_{CD} = 9,307 \text{ lbf/in.}$  Therefore, the associated error, calculated as:  $p_{Error} = [(p_{CD} - p_{Exp}^{Avg})/p_{Exp}^{Avg}] \times 100 = 12.63\%$ , is somewhat outside the pre-established  $\pm 10\%$  bounds, Figure 16, but, the difference is not significant. It is expected that refined models with smaller element sizes may result in the attainment of the peak load more consistent with experimental data.

On the other hand, the peak load predicted by FNM is  $p_{FNM} = 7748 \text{ lbf/in.}$  and therefore, the associated error, calculated as:  $p_{Error} = [(p_{FNM} - p_{Exp}^{Avg})/p_{Exp}^{Avg}] \times 100 = -6.23\%$ , is within the pre-established  $\pm 10\%$  bounds, Figure 16. The FNM code predicts increasing load-carrying capability in the post-peak regime, as shown by the

dotted green line. This may indicate that the delaminations and any matrix cracks have been arrested. Such a result, while contrary to experimental observations, most likely is an outcome of the modeling strategy wherein matrix cracking in the off-axis plies was ignored. This limitation would be overcome in future studies.

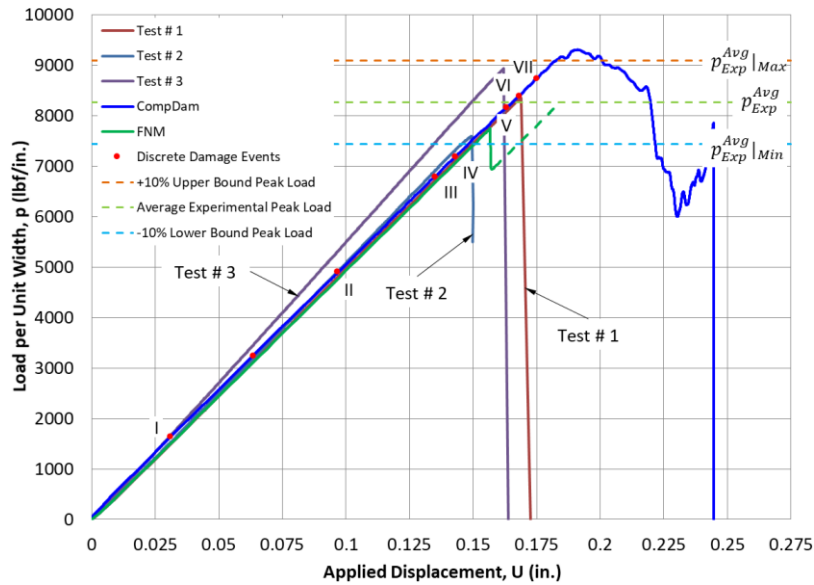


Figure 16. Load-displacement response of the pathfinder spar article computed as part of the static solution obtained with CompDam code.

The individual red dots labeled I through VII in the Figure 16 correspond to unique damage events predicted by the CompDam code at various displacement and load levels. The characteristic features of individual damage events are summarized in Table II. The locations mentioned in Table II are schematically illustrated in Figure 11.

TABLE II. DAMAGE EVENTS AND MODES

Damage Event	Damage Mode
I	Cracking at RP1/B2 interface, Figure 11
II	Delamination onset at B1/B2 interface; damage onset at the Tapered Interface
III	Matrix cracking onset in off-axis plies adjacent Symmetry Plane, Figure 12
IV	Matrix cracking onset in off-axis plies in Block # 3, Figure 11
V	Major delamination growth at B1/B2 interface; delamination migration to the B2/B3 interface
VI	Matrix cracking onset in off-axis plies in Block # 4, Figure 11
VII	Matrix cracking onset in off-axis plies in Block # 4, Figure 11 and continued growth of above damage modes

### Qualitative Comparisons of the Delamination Damage Mode

Under static testing, the damage events I through IV, Table II, could not be captured via UT imaging as the corresponding AE energy was not significant to warrant pausing the test. However, for damage event V, Table II, the test was paused and UT imaging was performed to obtain the shape of delamination growth. The correlations between CompDam predictions and experimental observations presented in Figure 17 (a) are reasonably good. In the post-peak regime, the CompDam code predicts extensive growth of delaminations, consistent with experimental observations.

On the other hand, correlations between FNM predictions and experimental observations, Figure 17 (b), may appear to be incongruous. However, it should be realized that the results in Figure 17 (b) are an outcome of the modeling strategies discussed in the previous sections and not a fundamental limitation of the code. Refined models, incorporating only FNM UELs and ABAQUS solid elements without native ABAQUS interfacial cohesive elements, are expected to yield better correlations.

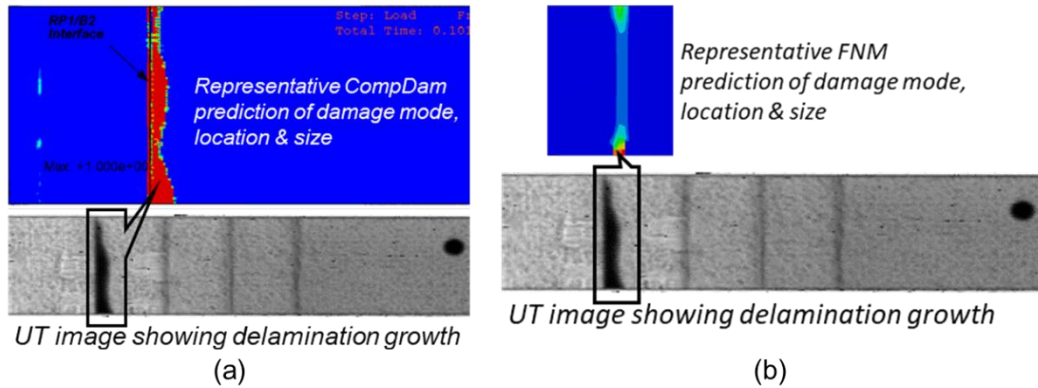


Figure 17. Qualitative correlations of predicted and experimentally observed delamination shapes.

Essentially, the damage events IV through VII, Figure 16, can be considered as near-peak behavior of the pathfinder test article under static tension loading. The cumulative effect of these damage events manifests as extensive delamination and matrix cracking in the off-axis composite plies. As seen from experimental observations, Figure 6, the block of core plies (Block # 1) and the block of belt plies (Block # 6), appear to have detached from the rest of the structure, whereas, matrix cracking appears confined to the central thin region of the pathfinder test article. Qualitative correlations between CompDam predictions and experimental observations of matrix cracking in the center-section along the off-axis ply directions presented in Figure 18 are reasonably good. The distinct bands of matrix cracks (red contours) presented in Figure 18, are a manifestation of setting the CompDam crack spacing parameter to 4.

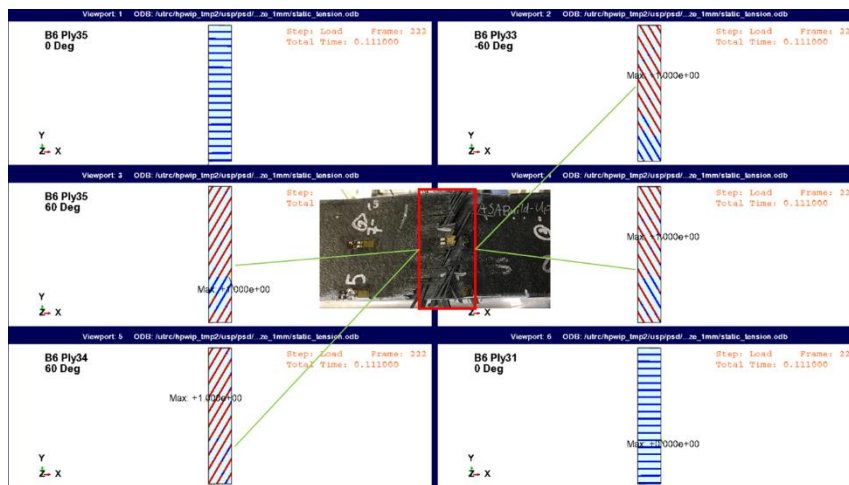


Figure 18. Correlations between CompDam predictions and experimental evidence on matrix cracking in off-axis plies.

## **DISCUSSIONS**

Continuing the previous work of the authors [9], detailed static and fatigue test data were obtained that demonstrated the ability to capture delamination onset and growth from the vicinity of ply-drops in tapered composite structures. Damage modes in such structures are often characterized by matrix cracking in the vicinities of manufacturing discontinuities such as ply-drops, which lead to large-scale delaminations. Experiments, both static and fatigue, performed as part of this work confirmed the above damage modes as documented via UT and C-Scan imaging. While the static load-displacement response indicated unstable fracture, UT imaging based on AE data successfully captured onset and growth of delaminations from the vicinities of the ply-drops. Since fatigue tests were performed at maximum cyclic loads of 55% – 60% of the average static peak load, progressive delamination growth from the vicinities of the ply-drops was successfully captured.

## **CONCLUSIONS**

This work endeavored to experimentally capture and computationally validate damage modes in tapered composite structures under static and cyclic tension loads. It was shown that the CompDam and FNM codes both predicted static pre-peak stiffness and peak load within  $\pm 10\%$  of corresponding experimental averages. Furthermore, it was shown that CompDam could predict the damage modes and their location and size in reasonable agreement with experimental data. The assumptions built into the FNM models of the tapered composite structures resulted in somewhat incongruous predictions of the size of delamination in the vicinity of the ply-drops. Overall, an integrated computational/experimental approach for capturing damage modes in tapered composite structures under static and fatigue loading conditions was successfully developed and demonstrated. Therefore, the V&V approach developed using the quasi-2D control specimen, appears promising for application of the same computational tools to the analysis of more complex, fully 3D composite structures.

## **ACKNOWLEDGEMENTS**

This material is based upon work supported by the National Aeronautics and Space Administration (NASA) under Award Nos. NNL09AA00A and 80LARC17C0004. Any opinions, findings, and conclusions or recommendations expressed in this material are those of the author(s) and do not necessarily reflect the views of NASA. Additional support received from the United Technologies Corporation (UTC) is gratefully acknowledged. The authors very much appreciate NASA ACP team members Drs. T. Kevin O'Brien, Cheryl A. Rose, Nelson V. De Carvalho, Frank A. Leone, Jr. Banavara R. Seshadri, and Mr. Gerald E. Mabson, Mr. Imran Hyder, Mr. William M. Johnston, Jr. and Mr. Joseph N. Zalameda for insightful discussions, pre- and post-processing of FE models, and generation and analysis of test data.

## REFERENCES

1. Krueger, R. 2010. "Development of a Benchmark Example for Delamination Fatigue Growth Prediction," NASA CR-2010-216723.
2. Krueger, R. 2011. "Development and Application of Benchmark Examples for Mode II Static Delamination Propagation and Fatigue Growth Predictions," NASA CR-2011-217305.
3. Krueger, R. 2012. "Development and Application of Benchmark Examples for Mixed-Mode I/II Quasi-Static Delamination Propagation Predictions," NASA CR-2012-217562.
4. De Carvalho, N.V., and R. Krueger. 2016. "Modeling Fatigue Damage Progression and Onset in Composites using an Element-Based Virtual Crack Closure Technique Combined with the Floating Node Method," in *Proceedings of the American Society for Composites 31st Technical Conference*, Williamsburg, VA, USA.
5. Wanthal, S., J. Schaefer, B. Justusson, I. Hyder, S. Engelstad and C. Rose. 2017. "Verification and Validation Process for Progressive Damage and Failure Analysis Methods in the NASA Advanced Composites Consortium," in *Proceedings of the American Society for Composites 32nd Technical Conference*, West Lafayette, IN.
6. Cui, X., X. Ren, P. Liu, J. Lua, P.M. Rao, M.D. Mordasky, and M.R. Gurvich. 2018. "A Dual Spring Modeling Approach for Static and Fatigue Failure Assessments of Carbon/Epoxy Composite Sub-Elements," *AIAA/ASCE/AHS/ASC Structures, Structural Dynamics, and Materials Conference*, 8–12 January 2018, Kissimmee, Florida.
7. Rao, P.M., M.D. Mordasky, M.R. Gurvich, N. de Carvalho, B.R. Seshadri, and J.G. Ratcliffe. 2018. "Validation of a Discrete Damage Mechanics Methodology Using the Static and Fatigue Behavior of Carbon/Epoxy Tapered Specimens," *AIAA/ASCE/AHS/ASC Structures, Structural Dynamics, and Materials Conference*, 8–12 January 2018, Kissimmee, Florida.
8. Seshadri, B.R., N.V. de Carvalho, L.R. Deobald, G.E. Mabson, and J.G. Ratcliffe. 2018. "Simulating the Clamped Tapered Beam Specimen under Quasi-Static and Fatigue Loading," *AIAA/ASCE/AHS/ASC Structures, Structural Dynamics, and Materials Conference*, 8–12 January, Kissimmee, Florida.
9. Rao, P.M., Palliyaguru, U.R., Gurvich, M.R., Seneviratne, W., An engineering approach to analyze damage initiation modes in tapered composite structures. - Proceedings of the American Society for Composites: Thirty-Third Technical Conference, Seattle, WA, September 24–26, 2018, p.2403-2418.
10. Leone, F. A. 2015. "Deformation Gradient Tensor Decomposition for Representing Matrix Cracks in Fiber-Reinforced Composite Structures," *Composites Part A: Applied Science and Manufacturing*, 76: 334–341.
11. Chen, B.Y., S.T. Pinho, N.V. De Carvalho, P.M. Baiz, and T.E. Tay. 2014. "A Floating Node Method for the Modelling of Discontinuities in Composites," *Engineering Fracture Mechanics*, 127:104–134.
12. Wisnom, M.R., R. Dixon and G. Hill. 1996. "Delamination in Asymmetrically Tapered Composites Loaded in Tension," *Composite Structures*, 35:309–322.
13. ABAQUS User's Manual. Dassault Systemes Simulia, Pawtucket, Rhode Island, USA.
14. Pinho, S.T., Davila, C.G., Camanho, P.P., Iannucci, L., et al. 2005. "Failure Models and Criteria for FRP Under In-Plane or Three-Dimensional Stress States Including Shear Non-Linearity," NASA Report NASA/TM-2005-213530.
15. Selvarathinam, A., J. Action, B. Justusson. Verification and Validation of Progressive Damage Analysis Methods for Explicit Analysis of Progressive Delamination, ASC 2017.